Article:
Radadiya, J., Rahman, A., Zhao, Y. et al. (2026) Low-excess-noise quinary AlGaInAsSb avalanche photodiodes on InP. Applied Physics Letters, 128 (25). 253306. ISSN: 0003-6951

https://doi.org/10.1063/5.0335508

Low-Excess-Noise Quinary AlGaInAsSb Avalanche Photodiodes on InP

J. Radadiya[1], A. Rahman[1], Y. Zhao[2], S. Zhao[2], H. Jung[1], J. P. R. David[2], and S. Lee[1,*]

[1]Department of Electrical Engineering, The University of Texas at Arlington, Arlington, Texas 76019, USA

[2]Department of Electronic and Electrical Engineering, University of Sheffield, Sheffield S1 3JD, UK

*Corresponding author: seunghyun.lee@uta.edu

Quinary AlGaInAsSb avalanche photodiodes lattice-matched to InP were demonstrated as low-noise multiplication layers. A 995 nm thick PIN $Al_{0.85}Ga_{0.07}In_{0.08}As_{0.63}Sb_{0.37}$ structure was grown on InP as a random alloy by molecular beam epitaxy. The devices exhibited breakdown at approximately -58 V, corresponding to a peak electric field of 628.8 kV/cm. Under 450 nm illumination, a maximum gain of 842 was achieved near breakdown with pure electron injection. Excess-noise measurements across multiple devices showed $F(M)$ values that were reproducibly low and deviated from the McIntyre local-field prediction, remaining below those of comparable $Al_{0.85}Ga_{0.15}As_{0.56}Sb_{0.44}$ and $Al_{0.79}In_{0.21}As_{0.74}Sb_{0.26}$ APDs at moderate and high gain. At $M \approx 70$, the effective k of AlGaInAsSb is approximately 0.01, compared with approximately ~0.022 and ~0.037 for AlGaAsSb and AlInAsSb, respectively. These results identify AlGaInAsSb as a promising quinary multiplication material for next-generation low-noise InP-based APDs and for potential application toward linear-mode single-photon detectors.

Avalanche photodiodes (APDs) are key detectors for low-light applications such as LiDAR imaging, sensing, and optical communication, including airborne and spaceborne platforms, because their internal avalanche gain amplifies weak input signals and can improve system signal-to-noise ratio.[1-3] This gain, M, however, is accompanied by excess noise due to the stochastic nature of impact ionization. According to McIntyre's local-field theory, the excess-noise factor, $F(M)$, for electron- or hole-initiated multiplication is given by,[4]

$$F(M) = kM + (1-k)\left(2 - \frac{1}{M}\right) \quad (1)$$

where $k = \beta/\alpha$ is the ratio of the hole and electron impact-ionization coefficients (by convention $k < 1$; for hole-initiated APDs, the analogous ratio is α/β).[4,5] Equation (1) shows that $F(M)$ is minimized when k approaches zero.[3-5] Because k is governed by the electronic band structure and carrier-scattering processes of the multiplication material, low-noise APD design is fundamentally a materials problem. Most efforts have therefore focused on electron-initiated APDs in which $\beta \ll \alpha$.

Heterostructure APDs based on a separate-absorption, grading, charge, and multiplication (SAGCM) architecture have been widely adopted in commercial technologies because the absorber and multiplier are separated both spatially and electrically. The grading and charge layers allow the electric fields in the absorber and multiplier to be optimized independently, helping to suppress tunneling current in the narrow-bandgap absorber while maintaining high avalanche gain in the multiplication region. For 1.55 μm detection on InP, commercial devices typically use an InGaAs absorber with either an InP or $Al_{0.48}In_{0.52}As$ (hereafter AlInAs) multiplier, both lattice matched to InP. However, their signal-to-noise ratio at high gain is limited by the relatively large excess noise, especially for $M > 10$, because the effective ionization-coefficient ratios remain significant: $k \approx 0.4$-0.5 for InP[5,6] and $k \approx 0.2$-0.3 for AlInAs.[7]

Over the past decade, Sb-based multipliers lattice-matched to InP, particularly $Al_xGa_{1-x}As_ySb_{1-y}$ and $Al_xIn_{1-x}As_ySb_{1-y}$, have emerged as promising alternatives to InP and AlInAs. $AlAs_{0.56}Sb_{0.44}$ provided a striking first example, with a reported k as low as 0.005[8]. Subsequent studies on $Al_{0.85}Ga_{0.15}As_{0.56}Sb_{0.44}$ (AlGaAsSb)[9-12] and $Al_{0.79}In_{0.21}As_{0.74}Sb_{0.26}$ (AlInAsSb)[13-15] also demonstrated very low excess noise, with k on the order of 10^{-2} at a low gain region ($M < 20$). However, the k values cannot be accurately determined for both AlGaAsSb and AlInAsSb because the measured $F(M)$ in Sb-based APDs does not follow the standard McIntyre local-field prediction, indicating that the impact-ionization statistics cannot be described completely by the simplest local-field picture.[11,16] A leading explanation for the low k is that the heavy Sb atom increases the valence-band spin-orbit splitting and introduces strong alloy-disorder scattering, thereby strongly suppressing hole impact ionization and driving β to very small values.[11,16,17] This interpretation is consistent with GaAsBi APDs, where small Bi incorporation substantially reduced k; for example, the effective k decreased from about 0.48 in GaAs to about 0.2 in GaAsBi with 4% Bi, and to about 0.15 in a thicker 4% Bi structure.[18]

More recently, there has been growing interest in pushing APD materials toward the limit $k \rightarrow 0$, particularly for single-photon and quantum-related applications.[19-22] In contrast to Geiger-mode single-photon avalanche diodes (SPADs), which operate above breakdown and require quenching and recovery, linear-mode SPADs aim to achieve very high but finite avalanche gain below breakdown.[2,19] In the ideal single-carrier limit ($\beta \approx 0$), very high linear-mode gain becomes possible without invoking Geiger operation.[2,20-22] HgCdTe and InAs electron-initiated APDs are important precedents, having demonstrated linear-mode photon counting or few-photon sensitivity.[2,20-22]

Against this background, the quinary AlGaInAsSb material system is a compelling platform to investigate. Relative to the quaternary Sb-based alloys, a quinary alloy provides an additional degree of compositional freedom to tune band gap and band alignment,[23] alloy disorder,[24,25] and potentially spin-orbit splitting. In particular, Indium (In) incorporation provides a linear grading scheme due to a favorable band alignment relative to InGaAs while retaining lattice matching to InP. This extra freedom is attractive for designing multiplication and grading layers compatible with InGaAs absorbers on InP, where heterointerface band offsets are an important design consideration.

In this paper, we investigate $Al_{0.85}Ga_{0.07}In_{0.08}As_{0.63}Sb_{0.37}$ (AlGaInAsSb) as a multiplication layer lattice matched to InP and compatible with InGaAs absorbers for 1.55 μm SAGCM APDs. The AlGaInAsSb APD exhibits very high gain ($M \approx 800$) near breakdown and a reduced effective k at high gain ($M > 50$) compared with AlGaAsSb and AlInAsSb APDs. These results indicate that AlGaInAsSb is a strong candidate for next-generation low-noise APDs on InP. More broadly, this work opens a path toward approaching the $k \rightarrow 0$ limit relevant to future linear-mode single-photon detectors and quantum photonic technologies.

Figure 1(a) shows the schematic structure of the p-i-n (PIN) AlGaInAsSb device. The PIN AlGaInAsSb structure was grown on epi-ready, on-axis InP substrates by molecular beam epitaxy (MBE). After careful calibration of the Al, Ga, and In growth rates using reflection high-energy electron diffraction, all layers were grown under conditions similar to those previously used for Sb-based multipliers on InP.[10] The full layer sequence and nominal thicknesses are described in TABLE I. The Secondary Ion Mass Spectroscopy (SIMS) doping profile (Figure S2 in Supplementary

Materials) also confirms that the dopant distribution and their concentration are consistent with the intended PIN structure.

TABLE I. Details of p-i-n AlGaInAsSb structure

Device Layer	Material	Width (nm)	Doping Type	Doping Concentration (cm^{-3})
Top contact	$In_{0.53}Ga_{0.47}As$	20	p^+	1×10^{-19}
p region	$Al_{0.85}Ga_{0.07}In_{0.08}As_{0.63}Sb_{0.37}$	300	p	2×10^{-18}
i region	$Al_{0.85}Ga_{0.07}In_{0.08}As_{0.63}Sb_{0.37}$	1000	i	UID
n region	$Al_{0.85}Ga_{0.07}In_{0.08}As_{0.63}Sb_{0.37}$	100	n	2×10^{-18}
Bottom contact	$In_{0.53}Ga_{0.47}As$	500	n^+	1×10^{-19}
Substrate	S.I. InP	--	--	

To perform the electrical and optical characterizations, circular mesa devices were fabricated using conventional photolithography and wet-chemical etching under conditions identical to those previously reported. For some devices, the sidewalls were additionally covered with a thin metal layer on top of the SU-8 passivation to reduce unwanted mixed injection from the sidewalls, as shown in the inset of Figure 1(a).

Figure 1(b) shows the measured X-ray diffraction (XRD) spectrum (ω-2θ scan) of the PIN AlGaInAsSb APD sample (black solid line). Four major peaks are observed. The central peak at 0 arcsec originates from the InP substrate. The peak at -210 arcsec is attributed to the InGaAs buffer/bottom-contact layer, as verified by the previous calibration run used to optimize the growth conditions. Two additional peaks were found to originate from the PIN AlGaInAsSb layers. The two AlGaInAsSb-related peaks are located at +173 and +300 arcsec. Assuming that the group-III fluxes (Al, Ga, and In) remained fixed during growth, that only the group-V fluxes changed, and that no significant relaxation occurred between the epitaxial layers and the InP substrate, the variation in As and Sb composition is estimated to be minimal, about 0.6% (less than 1%), corresponding to a compositional range from $Al_{0.85}Ga_{0.07}In_{0.08}As_{0.638}Sb_{0.362}$ to $Al_{0.85}Ga_{0.07}In_{0.08}As_{0.644}Sb_{0.356}$ which are deduced by the XRD simulation (blue solid line) as illustrated in Figure 1(b). This assumption is supported by the SIMS depth profile (Figure S1 in Supplementary Materials), which shows stable Al, Ga, and In signals across the PIN layers. In contrast, a small depth-dependent variation is observed in the group-V species, As and Sb. Therefore, the satellite features observed in the XRD scan are attributed primarily to slight As/Sb compositional variation rather than large-scale group-III segregation. The group-V variation is likely related to the very low As beam-equivalent pressure required for this alloy, below approximately 2×10^{-7} Torr, where precise flux control from the As cracker becomes challenging. In addition, As/Sb incorporation can be affected by growth transients and shutter operation, including the opening of the dopant shutter. These factors may lead to small fluctuations in the As/Sb composition during growth.

To evaluate the surface quality of the PIN AlGaInAsSb APD sample, Nomarski and atomic force microscopy (AFM) images were taken, as shown in Figure 2. The Nomarski image (50× magnification) reveals a very smooth surface morphology, while the AFM image shows an extremely low root-mean-square (RMS) roughness of 0.108 nm. These results indicate that high-quality growth of both the InGaAs and AlGaInAsSb layers was achieved.

To verify the band gaps of the AlGaInAsSb material, the quantum efficiency (QE) was measured at room temperature under a reverse bias of -5 V in order to determine the cutoff behavior corresponding to the material band gap, as shown in Figure 3(a). A reverse bias of −5 V was chosen for the QE measurement, corresponding to full device depletion and thus maximum QE at unity gain. This is supported by the capacitance saturation observed in the capacitance-voltage (C–V) curve in Figure 4(a). Because AlGaInAsSb is an indirect-bandgap material, its band gap is difficult to determine accurately by photoluminescence. In contrast, the QE spectrum near the absorption edge can be used to extract both the indirect and direct band gaps because, near cutoff, the QE follows the same photon-energy dependence as the absorption coefficient:[10,26-28]

$$QE \propto \left(E_{ph} - E_g\right)^n \quad (2)$$

where E_{ph} is the photon energy, E_g is the band gap, and n = 2 for an indirect transition[28] and n = 0.5 for a direct transition.[27] Therefore, the band gap can be determined accurately by linear fitting near the cutoff region of the QE spectrum. Accordingly, $QE^{0.5}$ and QE^2 were plotted as functions of photon energy, as shown in Figure 3(b) and 3(c), respectively. The x-intercepts of the linear fits indicate that the indirect and direct band gaps of the AlGaInAsSb alloy are 1.481 eV and 1.702 eV, respectively. These values are slightly lower than those previously reported for AlGaAsSb (indirect gap ≈ 1.52 - 1.56 eV and direct gap ≈ 1.77 eV).[9,10,26] This reduction is likely due to the combined effects of In incorporation, which lowers the band gap, together with increased alloy disorder in the quinary alloy system.

C-V measurements were performed on the PIN AlGaInAsSb devices with diameters of 100, 150, and 200 µm (hereafter D100, D150, and D200), as shown in Figure 4(a). The capacitance of all three devices scales perfectly with device area, confirming uniform material and device characteristics. Using an in-house 1D Poisson equation solver, the C-V model was fitted to the experimental C-V curves. The modeled C-V curves show excellent agreement with the measured data when assuming a UID layer thickness of 995 nm (almost similar to the 1000 nm nominal thickness), a background doping concentration of 5.6×10^{15} cm^{-3} in the UID layer, and doping concentrations of 2×10^{18} cm^{-3} in the p^+ and n^+ layers. The extracted layer parameters from the C-V model were further corroborated by the extracted doping profile, as shown in Figure 4(b), which closely matches the designed structure. In the modeling, a dielectric constant of 11.4 was used, corresponding to the average value estimated by interpolating the binary compounds, while accounting for small compositional fluctuations in the AlGaInAsSb layers based on the XRD results.

Figure 5(a) shows the current-voltage (I-V) curves under dark conditions for the devices with diameters of 150 and 200 µm (D150 and D200). Both devices show breakdown occurring at approximately -58 V, corresponding to a peak electric field of 628.8 kV/cm calculated from the 1D Poisson simulator.

To investigate the dominant dark-current contribution in the PIN AlGaInAsSb devices, the dark current of the four devices (D200, D250, D350, and D500) was plotted as a function of reverse bias voltage, as shown in Figure 5(b). The forward I-V curves exhibit an abrupt increase in current over a small bias range, indicating that the series resistance of the devices is relatively low. The ideality factors extracted from multiple devices range from 1.36 to 1.46 (average ~ 1.4), which lie between the ideal diffusion limit of 1 and the recombination-dominated limit of 2.

Using Eq (3) below, the bulk and dark current components can be extracted for any device diameters:

$$I_{total} = 2\pi r \times J_{surface} + \pi r^2 \times J_{Bulk} \quad (3)$$

Here, r is the device's radius. $J_{surface}$ is $I_{surface}$ per perimeter, and J_{bulk} is I_{bulk} per area (dark current density). Figure 5(c) shows the extracted $I_{surface}$ and I_{bulk} for D200. From 0 to -40 V, the $I_{surface}$ is an order of magnitude higher than the I_{bulk}. This suggests that the dominant dark-current component originates from the surface rather than the bulk. The likely origin of this surface leakage is non-ideal sidewall passivation, including etch-induced damage, dangling bonds, and local band bending at the passivated sidewall. This surface leakage increases dark-current noise, thereby degrading the device's sensitivity and detectivity. However, it is not expected to significantly affect the intrinsic excess-noise trend, because the $F(M)$ measurements were performed under optical injection, mainly through the active bulk region, and primarily reflect the impact-ionization statistics of photogenerated carriers. Further optimization of the sidewall treatment and passivation processes will be required to reduce surface leakage and improve device sensitivity.

Gain measurements were performed using an optical setup comprising a fiber-coupled 450 nm laser, coupled into the optical window of the processed devices via a lensed fiber. The smallest diameter of the laser beam is approximately 50 μm, which is significantly smaller than the device diameters used in this study, ensuring that no mixed injection profile occurs. From linear interpolation of related alloy optical constants of binary constituents,[29-31] the absorption coefficient of AlGaInAsSb at 450 nm was estimated to be 2.12×10^5 cm^{-1}. Therefore, the 300 nm p+ top cladding layer is sufficient to provide pure electron injection because the optical intensity decays to approximately 0.17% of the incident intensity according to Beer-Lambert's law.

Figure 6(a) shows the measured I-V characteristics under dark conditions (black solid line) and under 450 nm illumination (black short-dashed line) for the D200 device. By subtracting the dark current from the illuminated current, the pure photocurrent can be obtained. Using Woods' correction (baseline correction)[32], the gain (blue circular markers) was extracted from the photocurrent curve. To verify the accuracy of the calculated gain curve, the gain measurements were repeated at different laser intensities ranging from 0.059 to 0.824 μW. As shown in Figure 6(b), the extracted gain curves are nearly identical over this intensity range, confirming the reliability of the gain extraction method. A maximum gain of 842 was achieved near the breakdown voltage. This result demonstrates that the PIN AlGaInAsSb APD can achieve a very high multiplication gain of nearly 3 orders of magnitude prior to breakdown, indicating its potential for high-performance single-photon LiDAR systems and linear-mode SPADs for quantum technology applications.

The $F(M)$ of the PIN AlGaInAsSb APD was measured using an excess-noise measurement setup consisting of an in-house circuit equipped with a 455 nm fiber-coupled LED, a mechanical chopper, and two lock-in amplifiers. The detailed configuration of the setup was similar to that described here[33]. The measured $F(M)$ values were cross-checked using a noise figure meter equipped with a bias tee and a source meter unit under 450 nm laser illumination using GSG probes to ensure the accuracy of the extracted $F(M)$.

Figure 7 shows the measured $F(M)$ of the 995 nm-thick PIN AlGaInAsSb APDs for three different D200 devices (Device 1, Device 2, and Device 3) as a function of gain. These three $F(M)$ curves represent results obtained from three separate sets of multiple devices. For comparison, the $F(M)$ results are also plotted alongside Si[34], InP[5,6], AlInAs[7], and those of a 1020 nm-thick PIN AlGaAsSb APD[11] and a 997 nm-thick PIN AlInAsSb APD[14]; because the AlGaAsSb and AlInAsSb data are not available in the high-gain region ($M > 38$), the corresponding trends in this region are extrapolated and shown as dashed lines. The other dashed curves represent the theoretical predictions from McIntyre's local-field theory (Eq. 1), showing $F(M)$ calculated for k values ranging from 0 to 0.1 in steps of 0.01.

The measured $F(M)$ of the three PIN APDs do not follow the prediction of McIntyre's local-field theory. This indicates that the excess noise characteristics of Sb-based quaternary and quinary materials cannot be fully described by the conventional local-field model, which assumes the ionization probability distribution follows a simple exponential form and that excess noise is determined by the local ionization-coefficient ratio. Non-local descriptions, including dead-space[35], history-dependent[36], and Monte Carlo models[37], have shown that the ionization probability distribution function can be modified by the carrier's previous transport history, leading to a more deterministic avalanche process and reduced excess noise. However, the multiplication regions studied here are relatively thick, approximately 1000 nm, so conventional dead-space effects alone are expected to be small. The low excess noise observed in these Sb-containing alloys, therefore, suggests that additional material-dependent transport effects may be important. In particular, alloy disorder, local potential fluctuations, and modified band structure may influence how carriers gain and lose energy before impact ionization. The incorporation of In in the quinary AlGaInAsSb alloy may further modify this ionization probability distribution, reducing $F(M)$ while leaving the mean multiplication characteristics largely unchanged. Thus, a more complex electric-field-dependent probability density function[38-40] is likely required to accurately describe the avalanche process in these materials.

A small difference in $F(M)$ between the two AlGaInAsSb devices (1^{st} and $2^{nd}/3^{rd}$) is observed, which may originate from slight compositional variations or small differences in depletion width caused by nonuniform dopant diffusion across the wafer. Error bars corresponding to a 5% uncertainty have been added to the measured $F(M)$ data points in Figure 7. Nevertheless, the overall agreement between the three devices is very good, indicating that the measured $F(M)$ characteristics are highly reproducible. While phase instability in this quinary alloy system may introduce compositional variability, affecting device uniformity and manufacturability, its impact appears limited here, as suggested by the generally good agreement in the measured characteristics.

The $F(M)$ of the PIN AlGaInAsSb APDs is significantly lower than that of InP and AlInAs, and similar to or slightly lower than that of the PIN AlGaAsSb and PIN AlInAsSb APDs in the low-gain region ($M < 15$). However, the difference between the three materials becomes more pronounced as the gain increases beyond $M = 15$. For example, at $M = 15$, 20, and 30, the $F(M)$ values of the PIN AlGaInAsSb/PIN AlGaAsSb/PIN AlInAsSb APDs are about 1.56/1.74/2.00, 1.66/1.85/2.22, and 1.83/2.24/2.6, respectively, indicating that the discrepancy increases with gain. At

M = 60-63, the effective k values of the PIN AlGaInAsSb, PIN AlGaAsSb, and PIN AlInAsSb APDs are approximately 0.01, 0.02, and 0.035, respectively. Furthermore, the $F(M)$ of PIN AlGaInAsSb is approximately 1.4 times lower than that of the PIN Si at M = 60-63, despite having an avalanche region that is approximately five times thinner.

These results clearly indicate that incorporating In into AlGaAsSb modifies the electronic band structure and carrier-scattering mechanisms. This behavior is likely due to a combination of factors, including modifications of the bandgap, band alignment, alloy-disorder scattering, and valence-band spin-orbit splitting. These effects could influence the relative electron and hole impact-ionization rates, thereby reducing the effective ionization-coefficient ratio k. However, we note that this interpretation is currently qualitative. A quantitative confirmation would require first-principles band-structure calculations combined with Monte Carlo transport simulations that explicitly account for alloy-disorder scattering and nonlocal impact-ionization processes in the AlGaInAsSb alloy. Such calculations are beyond the scope of the present work and will be pursued in future studies.

Overall, the $F(M)$ of the PIN AlGaInAsSb APDs exhibits very low excess-noise behavior even in the high-gain region, indicating that this quinary material system is a strong candidate for next-generation multiplication layers, with potential applications toward low-noise, single-photon-level detection, although experimental validation of single-photon detection capability remains to be demonstrated.

In conclusion, MBE-grown 995 nm-thick PIN AlGaInAsSb APDs, nearly lattice-matched to InP, were demonstrated and evaluated as low-noise multiplication layers. Under pure electron injection at 450 nm, the APDs achieved a gain of up to 842 near the breakdown voltage of -58 V. Excess-noise measurements on multiple devices showed reproducibly low $F(M)$ and a clear advantage over AlGaAsSb at higher gain, with an effective k of approximately 0.01 at $M \approx$ 60-63. Overall, AlGaInAsSb combines high gain with very low excess noise and is therefore, it is a strong candidate for next-generation multiplication layers in InP-based APDs, with potential applications toward low-noise detection approaching the single-photon level and future linear-mode SPAD technologies.

SUPPLEMENTARY MATERIAL

SIMS elemental, dopant, and impurity depth profiles confirming the AlGaInAsSb APD layer structure and compositional uniformity, as well as additional excess-noise measurements showing the effects of illumination wavelength, optical spot size, mesa diameter, and sidewall metal coverage.

ACKNOWLEDGMENTS

The author would like to sincerely thank Dr. Sadhvikas Addamane at Sandia National Laboratories for his valuable support and contributions to the initial work on optimizing the fabrication of detector devices using InGaAs layers. The author also gratefully acknowledges IntelliEPI Inc. for providing the initial wafers that enabled this research. Furthermore, this work was performed, in part, at the Center for Integrated Nanotechnologies, an Office of Science User Facility operated for the U.S. Department of Energy (DOE) Office of Science by Los Alamos National Laboratory (Contract 89233218CNA000001) and Sandia National Laboratories (Contract DE-NA-0003525).

AUTHOR DECLARATIONS

Conflict of Interest

The Authors have no conflicts to disclose.

Author Contributions

J.R and A.R. contributed equally to this paper.

DATA AVAILABILITY

The data that support the findings of this study are available from the corresponding author upon reasonable request.

REFERENCES

[1] J. C. Campbell, J. Lightwave Technol. 25, 109 (2007).

[2] X. Sun, J. B. Abshire, J. D. Beck, P. Mitra, K. Reiff, and G. Yang, Optics Express 25, 16589 (2017).

[3] X. Sun, Sensors 24, 6620 (2024).

[4] R. J. McIntyre, IEEE Trans. Electron Devices 13, 164 (1966).

[5] J. C. Campbell, IEEE J. Sel. Top. Quantum Electron. 28, 3800911 (2022).

[6] L. J. J. Tan, J. S. Ng, C. H. Tan, and J. P. R. David, IEEE J. Quantum Electron. 44, 378 (2008).

[7] Y. L. Goh, A. R. J. Marshall, D. J. Massey, J. S. Ng, C. H. Tan, and M. Hopkinson, IEEE J. Quantum Electron. 43, 503 (2007).

[8] X. Yi, S. Xie, B. Liang, L. W. Lim, J. S. Cheong, M. C. Debnath, D. L. Huffaker, C. H. Tan, and J. P. R. David, Nat. Photonics 13, 683 (2019).

[9] S. Lee, S. H. Kodati, B. Guo, A. H. Jones, M. Schwartz, M. Winslow, C. H. Grein, T. J. Ronningen, J. C. Campbell, and S. Krishna, Appl. Phys. Lett. 118, 081106 (2021).

[10] S. Lee, B. Guo, S. H. Kodati, H. Jung, M. Schwartz, A. H. Jones, M. Winslow, C. H. Grein, T. J. Ronningen, J. C. Campbell, and S. Krishna, Appl. Phys. Lett. 120, 071101 (2022).

[11] S. Lee, X. Jin, H. Jung, H. I. J. Lewis, Y. Liu, B. Guo, S. H. Kodati, M. Schwartz, C. H. Grein, T. J. Ronningen, J. P. R. David, J. C. Campbell, and S. Krishna, Optica 10, 147 (2023).

[12] H. Jung, S. Lee, X. Jin, Y. Liu, T. J. Ronningen, C. H. Grein, J. P. R. David, and S. Krishna, Commun. Mater. 5, 219 (2024).

[13] S. H. Kodati, S. Lee, B. Guo, A. H. Jones, M. Schwartz, M. Winslow, N. A. Pfiester, C. H. Grein, T. J. Ronningen, J. C. Campbell, and S. Krishna, Appl. Phys. Lett. 118, 091101 (2021).

[14] T. J. Ronningen, S. H. Kodati, X. Jin, S. Lee, H. Jung, X. Tao, H. I. J. Lewis, M. Schwartz, and N. Gajowski, Appl. Phys. Lett. 123, 131101 (2023).

[15] B. Guo, M. Schwartz, S. H. Kodati, K. M. McNicholas, H. Jung, S. Lee, J. Konowitch, D. Chen, J. Bai, and X. Guo, APL Photon. 8, 116112 (2023).

[16] H. I. J. Lewis, X. Jin, B. Guo, S. Lee, H. Jung, S. H. Kodati, B. Liang, S. Krishna, D. S. Ong, and J. C. Campbell, Sci. Rep. **13**, 9936 (2023).

[17] J. C. Campbell, J. P. R. David, and S. R. Bank, Photonics 10, 715 (2023).

[18] Y. Liu, X. Yi, N. J. Bailey, Z. Zhou, T. B. O. Rockett, L. W. Lim, C. H. Tan, R. D. Richards, and J. P. R. David, Nat. Commun. **12**, 4784 (2021).

[19] S. Cova, M. Ghioni, A. Lacaita, C. Samori, and F. Zappa, Appl. Opt. 35, 1956 (1996).

[20] J. Beck, C. Wan, M. Kinch, J. Robinson, P. Mitra, R. Scritchfield, F. Ma, and J. C. Campbell, J. Electron. Mater. **35**, 1166 (2006).

[21] A. R. J. Marshall, J. P. R. David, and C. H. Tan, IEEE Trans. Electron Devices 57, 2631 (2010).

[22] C. H. Tan, A. Velichko, L. W. Lim, and J. S. Ng, Opt. Express 27, 5835 (2019).

[23] G. Belenky, L. Shterengas, G. Kipshidze, and T. Hosoda, IEEE J. Sel. Top. Quantum Electron. 17, 1426 (2011).

[24] S. Emura, K. Koto, A. Yoshiasa, H. Ito, S. Gonda, and S. Mukai, J. Mater. Sci. Lett. 8, 1236 (1989).

[25] L. H. Li, V. Sallet, G. Patriarche, L. Largeau, S. Bouchoule, L. Travers, and J. C. Harmand, Appl. Phys. Lett. 83, 1298 (2003).

[26] X. Zhou, S. Zhang, J. P. R. David, J. S. Ng, and C. H. Tan, IEEE Photonics Technol. Lett. 28, 2495 (2016).

[27] L. H. Hall, J. Bardeen, and F. J. Blatt, Phys. Rev. 95, 559 (1954).

[28] M. Fox, Optical Properties of Solids (Oxford University Press, 2010).

[29] A. D. Rakić and M. L. Majewski, J. Appl. Phys. 80, 5909 (1996).

[30] S. Adachi, J. Appl. Phys. 67, 6427 (1990).

[31] S. Adachi, J. Appl. Phys. 66, 6030 (1989).

[32] M. H. Woods, W. C. Johnson, and M. A. Lampert, Solid-State Electron. 16, 381 (1973).

[33] K. S. Lau, C. H. Tan, B. K. Ng, K. F. Li, R. C. Tozer, J. P. R. David, and G. J. Rees, Meas. Sci. Technol. 17, 1941 (2006).

[34] Hamamatsu, Si APD, S12023 Series (Hamamatsu Photonics, 2022).

[35] M. M. Hayat, B. E. A. Saleh, and M. C. Teich, IEEE Trans. Electron Devices 39, 546 (1992).

[36] R. J. McIntyre, IEEE Trans. Electron Devices 46, 1623 (2002).

[37] D. S. Ong, K. F. Li, S. A. Plimmer, G. J. Rees, J. P. R. David, and P. N. Robson, J. Appl. Phys. 87, 7885 (2000).

[38] D. S. Ong, A. H. Tan, K. Y. Choo, K. H. Yeoh, and J. P. R. David, J. Phys. D: Appl. Phys. 55, 065105 (2022).

[39] D. S. Ong, X. Jin, K. H. Yeoh, A. H. Tan, K. Y. Choo, and J. P. R. David, J. Phys. D: Appl. Phys. 59, 025103 (2026).

[40] D. S. Ong, A. H. Tan, X. Jin, and J. P. R. David, Semicond. Sci. Technol. 40, 125011 (2025).

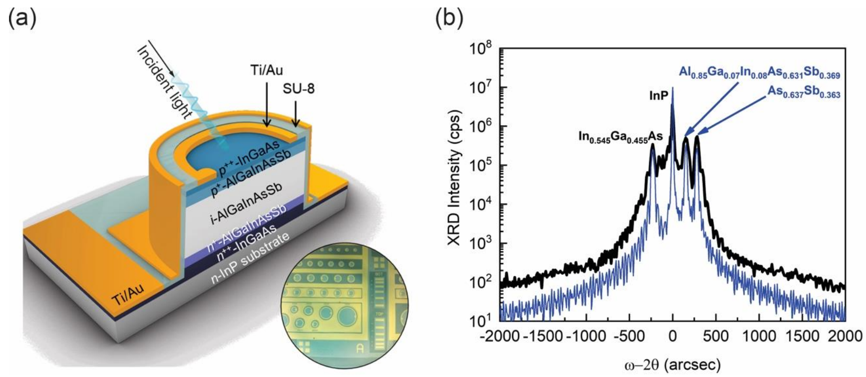

FIG. 1. (a) Schematic structure of the PIN AlGaInAsSb APD and sidewall metallization scheme used for pure electron-injection measurements. (b) Measured (black solid line) and simulated (blue solid line) X-ray diffraction ω-2θ scans of the PIN AlGaInAsSb structure.

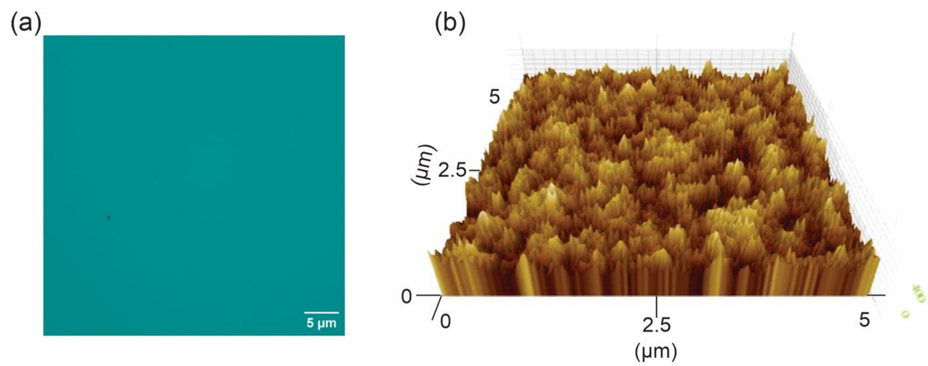

FIG. 2. Nomarski and AFM images of the PIN AlGaInAsSb surface. The AFM image gives an RMS roughness of 0.108 nm.

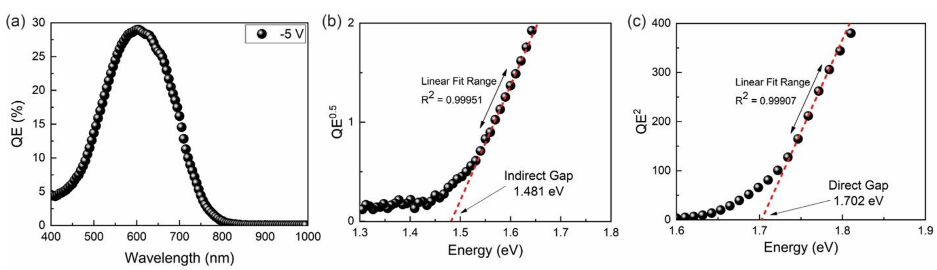

FIG. 3. (a) Quantum efficiency spectrum of the PIN AlGaInAsSb APD measured at room temperature under -5 V reverse bias. (b) $QE^{0.5}$ versus photon energy for extraction of the indirect band gap. (c) QE^2 versus photon energy for the extraction of the direct band gap.

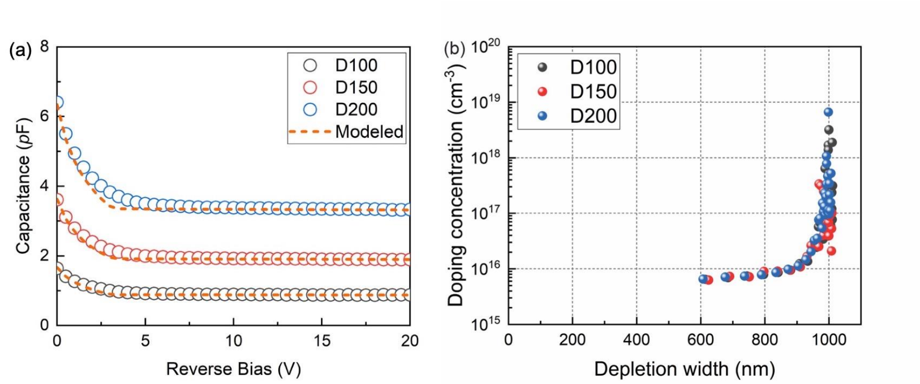

FIG. 4. (a) Capacitance-voltage characteristics of the 100, D150, and D200 devices together with the fitted 1D Poisson CV model. (b) Extracted doping profile of the PIN AlGaInAsSb structure.

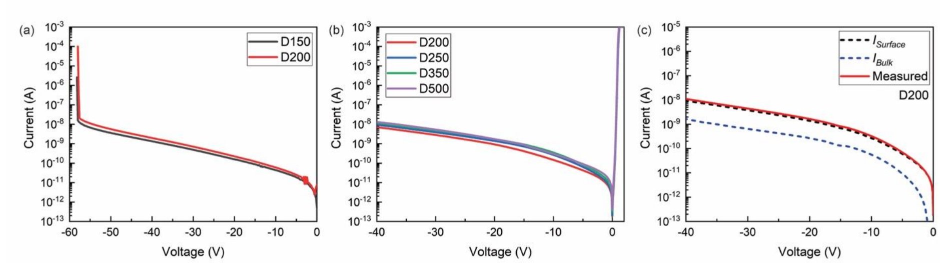

FIG. 5. (a) Dark current-voltage characteristics of the D150 and D200 devices. (b) Dark current-voltage characteristics of the D200, D250, D350, and D500 to investigate the dark current contributions. (c) Extracted $I_{surface}$ and I_{bulk} for D200 as a function of voltage.

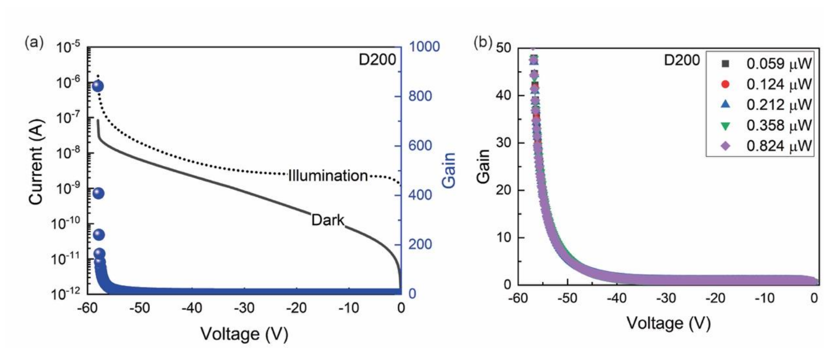

FIG. 6. (a) Dark current, illuminated current, and extracted gain for the D200 device under 450 nm illumination. (b) Gain curves extracted at different laser intensities ranging from 0.059 to 0.824 μW.

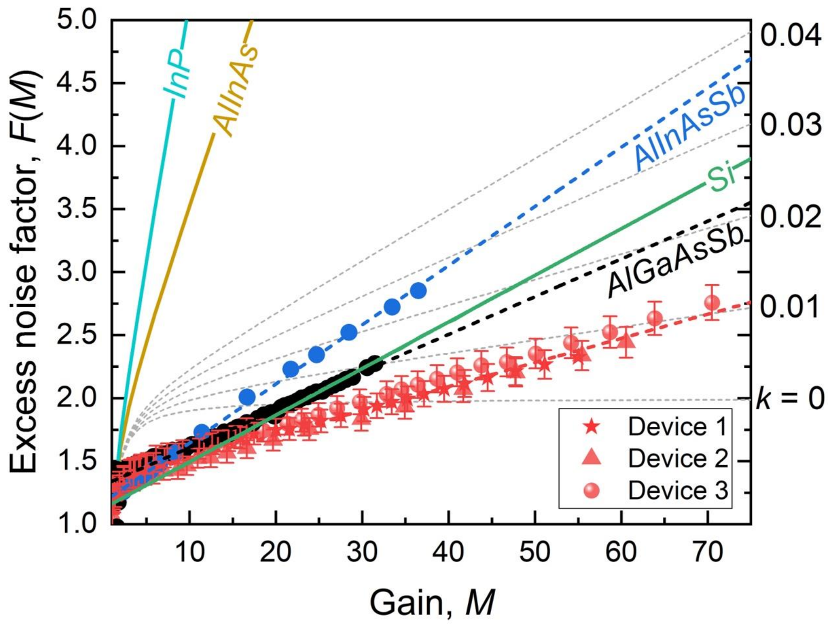

FIG. 7. Excess noise factor, $F(M)$, as a function of gain for 995 nm-thick PIN AlGaInAsSb APDs measured on three sets of D200 devices. Results are compared with Si[34], InP[5,6], AlInAs[7], and those of a 1020 nm-thick PIN AlGaAsSb[11] and a 997 nm-thick PIN AlInAsSb APD[14]. Dashed curves show McIntyre's local-field predictions for various k from 0 to 0.04, with a step of 0.01; the high-gain AlGaAsSb and AlInAsSb trends are extrapolated where data are unavailable.